Applied Catalysis B: Environmental 108–109 (2011) 32–38

Contents lists available at ScienceDirect

Applied Catalysis B: Environmental

journal homepage: www.elsevier.com/locate/apcatb

Improvement of oxygen storage capacity using mesoporous ceria–zirconia solid solutions

Sara Abdollahzadeh-Ghom[a,b,*], Cyrus Zamani[a], Teresa Andreu[b], Mauro Epifani[c], J.R. Morante[a,b]

[a] M-2E/IN²UB, Dept. Electrònica, Universitat de Barcelona, Barcelona 08028, Spain
[b] IREC, Catalonia Institute for Energy Research, Jardins de les Dones de Negre, 1, 08930 Sant Adrià del Besòs, Barcelona 08019, Spain
[c] Istituto per la Microelettronica e i Microsistemi, IMM-CNR, Sezione di Lecce, Via Arnesano, 73100 Lecce, Italy

ARTICLE INFO

Article history:
Received 22 May 2011
Received in revised form 21 July 2011
Accepted 26 July 2011
Available online 22 August 2011

Keywords:
Mesoporous
Ceria
Zirconia
KIT-6
SBA-15
Oxygen storage capacity
Hard template

ABSTRACT

Mesoporous phases of ceria (CeO_2) and ceria–zirconia solid solutions up to 50% of Zr have been synthesized using hard template method. The structures of the obtained metal oxides replicas correspond to the chosen structures of the KIT-6 and SBA-15 silica. This method allows obtaining materials with a uniform and homogenous porous size distribution as replica of the used nanotemplate. This structure facilitates the interaction with the gas molecules, their diffusivity inside the material and the porous size control. Obtained replicas were analysed using a variety of characterization techniques. TEM results reveal successful formation of the expected structures which were also supported by BET measurements. Replicas obtained applying SBA-15 and KIT-6 nanotemplates present similar behaviour although KIT-6 shows a slightly higher (about 5%) active surface with values in the range of 125 m^2/g after thermal annealing. XRD and Raman spectra confirm formation of solid solutions with cubic structure up to 20% of zirconium above which, formation of tetragonal phase was observed. Functionally, besides their high active surface, these ceria–zirconia solid solutions show significant improvement in their oxygen storage capacity (OSC). In comparison with pure mesoporous ceria, it has been found that due to the introduction of zirconium even for a few percentage of zirconium (5%) the OSC increases (more than 30 times) which is attributed to the presence of substitutional zirconium in the ceria lattice.

1. Introduction

Ceria (CeO_2) has significant oxygen ionic conduction at lower temperatures as compared to pure zirconia [1] and according to its redox properties, it has a fast Ce^{4+}/Ce^{3+} balance [2] which can be simply written as:

$$2CeO_2 \leftrightarrow Ce_2O_3 + \frac{1}{2}O_2 \quad (1)$$

As a consequence, for its use in three way catalysts, ceria can store O_2 during an oxygen-rich phase and later, feed the noble metal with oxygen when the O_2 partial pressure decreases. This capability for feeding oxygen is estimated according to the value of the oxygen storage capacity, OSC, which determines its role in the optimum CO, HC, and NO_x conversions [3]. This property is lost as the temperature increases. So, thermal stability at high temperature becomes an essential requirement taking into account that it must be applied in the flue duct of many combustion chambers or internal combustion engines with operating temperatures higher than 700 °C [4]. Likewise, the oxygen storage capacity needs to be increased since thermodynamically, solid ceria in its pure form, crystallizes in the fluorite structure co-ordinating each cerium atom with 8 neighbouring oxygens. This results in stabilization of the material, making the CO_2 reduction unfavourable. Therefore, materials should be modified in order to improve these performances. Under these restrictive boundaries, as ZrO_2 has better stability at higher temperatures, binary compounds, $Ce_xZr_{1-x}O_2$, constitutes an interesting alternative for satisfying all of these requirements, thermal stability and oxygen storage capability, in a wide operating window. In fact, introduction of some zirconium atoms in the ceria lattice by isomorphous substitution of Ce^{4+} cations (ionic radius 0.97 Å) with Zr^{4+} cations (ionic radius 0.84 Å), clearly should influence the final properties of these materials, at least, as long as the cubic structure of ceria is maintained [5,6]. This is a result of introduction of extrinsic defects associated with oxygen vacancies which in Kröger–Vink notation is stated as:

$$ZrO_2 = Zr'_{Ce} + V_O^{\bullet\bullet} + 2O_O^{\times} \quad (2)$$

Vacancies can also be created as a result of surface interactions with oxygen which means that surface oxygen density is a function of the oxygen partial pressure:

$$2Ce_{Ce}^{\times} + O_O^{\times} = 2Ce'_{Ce} + V_O^{\bullet\bullet} + \tfrac{1}{2}O_2 \quad (3)$$

* Corresponding author.
E-mail address: sarayehamid@yahoo.com (S. Abdollahzadeh-Ghom).

0926-3373/$ – see front matter © 2011 Elsevier B.V. All rights reserved.
doi:10.1016/j.apcatb.2011.07.038

On one hand, higher oxygen bulk mobility is expected due to the zirconium presence and, on the other hand, there is a higher surface oxygen vacancy due to the lattice parameter changes. Both features are enhancing the oxygen storage capacity.

Nevertheless, it is well known that all of these properties are changed for nanocrystalline materials. For example, nanocrystalline ceria, about 10 nm or less in size, possesses greatly reduced grain boundary impedance and increased electronic conductivity [7,8]. Fundamental defect and transport properties govern these properties and, hence, the dominant role of interfacial defect formation gives rise to preferential reduction at grain boundary atomic sites of lowered oxygen vacancy formation energy. The concentration of oxygen vacancies is changed two orders of magnitude when the crystal size is increased from 4 to 60 nm. All such properties fundamentally depend on the defect thermodynamics and related electrical and mass transport properties of the polycrystalline solid that are strongly dependent on the synthesis and treatment procedures. For example, Conesa group showed that fabrication of these mixed oxides through microemulsion method can result in 2D or 3D structures with different phases (pseudo-cubic t″ phase in high concentrations of Ce) which differ in catalytic properties [9]. Therefore, the origin of many of the reported data for nanocrystalline oxides is unclear whether they are due to (i) increased interfacial area, (ii) logical extensions of conventional size scaling laws (e.g., the grain size dependence of oxygen diffusion), or (iii) the result of truly size-dependent physical properties as the oxygen vacancy enthalpy of formation [10]. So, different results have been reported for different synthesis procedures like sol–gel [11] and mechanical milling [12] pointing out the strong sensitivity of the interfacial characteristics to the obtaining procedure, especially thermal treatment, and its control.

A variety of processes have been reported for preparation of ceria–zirconia solid solutions [13,14]. In this work, we report a procedure based on the use of mesoporous silica as a hard template for the synthesis of mesoporous ceria–zirconia solid solutions. The use of templates is an attractive alternative to overcome the abovementioned difficulties concerning the fabrication control and its influence on the interfacial properties as nanoparticle properties become related to the used template. Nevertheless, the soft-template methods, based on the use of surfactants, were initially discarded because the template is removed before annealing and this introduces difficulties for preventing the material agglomeration. In contrast, in the hard-template methods, the template is removed afterwards, and this ensures a good control of the particle size since the template acts as a physical barrier to coalescence of the crystals during the calcination process. The hard-template method also offers several additional advantages. Firstly, it allows obtaining a porous network that depends on the nanotemplate structure, selected among a wide variety, such as MCM-41, SBA-15, KIT-6, and SBA-16. Secondly, the replication process using silica templates is easy to scale-up. This is an advantage compared with other hard-templates such as anodized aluminum oxides (AAO) membranes [15]. Thirdly, mesoporous silica templates offer good thermal stability for the synthesis of metal oxides compound even at relatively high temperatures [16].

2. Experimental

2.1. Synthesis of nanotemplates

Mesoporous silica was synthesised using a non-ionic triblock copolymer surfactant ($EO_{20}PO_{70}EO_{20}$, Pluronic P123 from BASF®) as a structure directing agent. In this work, we have used two different structures of mesoporous silica: SBA-15 (two-dimensional hexagonal *p6mm* symmetry) and KIT-6 (three-dimensional cubic *Ia3d* symmetry).

For the preparation of SBA-15 [16,17], 6 g of P123 were dissolved in 60 g of HCl (6 M) and 165 g of deionized H_2O, stirring for 4–6 h at constant temperature of 38 °C in a thermal bath. Then, 12.49 g of tetraethylorthosilicate (TEOS, 98%, Aldrich) was added drop wise. The resulting mixture was stirred again for 24 h at 38 °C in the thermal bath. A hydrothermal treatment was performed on the product through putting the sample in an oven already heated up to 100 °C for another 24 h. Samples were then filtered and cleaned with purified water. This step was followed by a drying process in oven at 50–60 °C for 24 h. Resulting nanopowder was finally calcined at 550 °C for 4 h using a heating ramp of 4 °C/min.

Similarly, KIT-6 [16,18] was prepared in the same way through mixing 6 g of P123 with 24 g HCl and 208 g H_2O. Here, after 2 h of stirring at 36 °C, 6 g of 1-butanol was added followed by 3 h of stirring. Then, 12.49 g TEOS was added and the agitation was continued for another day at 36 °C. Hydrothermal treatment was performed at 90 °C for 24 h. The rest of the process was the same as the one used for SBA-15.

2.2. Synthesis of mesoporous ceria and ceria–zirconia

Solid solutions of ceria–zirconia were prepared by a two-step impregnation method where the previously synthesised silica templates were impregnated with aqueous solutions of its nitrate salts [16].

First, proper amounts of cerium nitrate ($Ce(NO_3)_3{\cdot}6H_2O$) and zirconium oxynitrate ($ZrO(NO_3)_2{\cdot}6H_2O$) were dissolved in purified water in order to make 0.1 M solutions. In the first impregnation step, 0.15 g of silica template (SBA-15 or KIT-6) was mixed with the adequate volumes of ceria and zirconia solutions in order to have 1 mmol of total metal ions. The metal ratio $[Zr^{4+}]/([Zr^{4+}]+[Ce^{3+}])$ was varied between 0 and 0.5. The mixture was stirred for 30 min, dried at 50 °C and calcined at 350 °C for 4 h with a heating rate of 4 °C/min. In the second impregnation step, 0.5 mmol of metal ions ($[Zr^{4+}]+[Ce^{3+}]$) with the same metal ratio were added to the resulting powder, stirred, dried and calcined to the final calcination temperature (600 °C, 800 °C or 1000 °C).

To remove the template, products were hot-etched using NaOH. Powders were introduced in a 2 M NaOH solution and stirred for 24 h at 70 °C. Products (ceria and ceria–zirconia powders with mesoporous structure) were recovered by centrifugation and cleaned several times with purified water until reaching a neutral product (pH 7). They were finally washed with ethanol for two times and oven-dried for 12 h in air.

2.3. Characterization

XRD analysis was performed on Siemens D500 and Bruker D4 X-ray Powder diffractometers, working with the Cu Kα radiation with Bragg Brentano geometry. TEM characterization was carried out using a Philips CM30 SuperTwin electron microscope operating at 300 keV. BET (Brunauer–Emmett–Teller) analysis was performed using a Micromeritics Tristar 3000 surface area analyzer, degassing the samples at 150 °C before doing the experiment. Raman spectra were recorded at room temperature using a Jobin Yvon T64000 spectrograph equipped with a bidimensional charge-coupled device (CCD) detector and an Ar^+ Coherent INNOVA 300 laser ($\lambda = 514$ nm) as excitation source. The laser power onto the sample was 3 mW.

Oxygen storage capacity was measured by thermogravimetric analysis (TG) [11], using a thermobalance TGA-SDTA 851e/SF/1100 from Mettler Toledo. 15 mg of mesoporous ceria or ceria–zirconia powder was heated up to 600 °C in nitrogen (50 mL/min) in order to release oxygen from the sample. After 10 min of stabilization, synthetic air was introduced resulting to an increase in sample weight due to the uptake of oxygen from air. This weight change

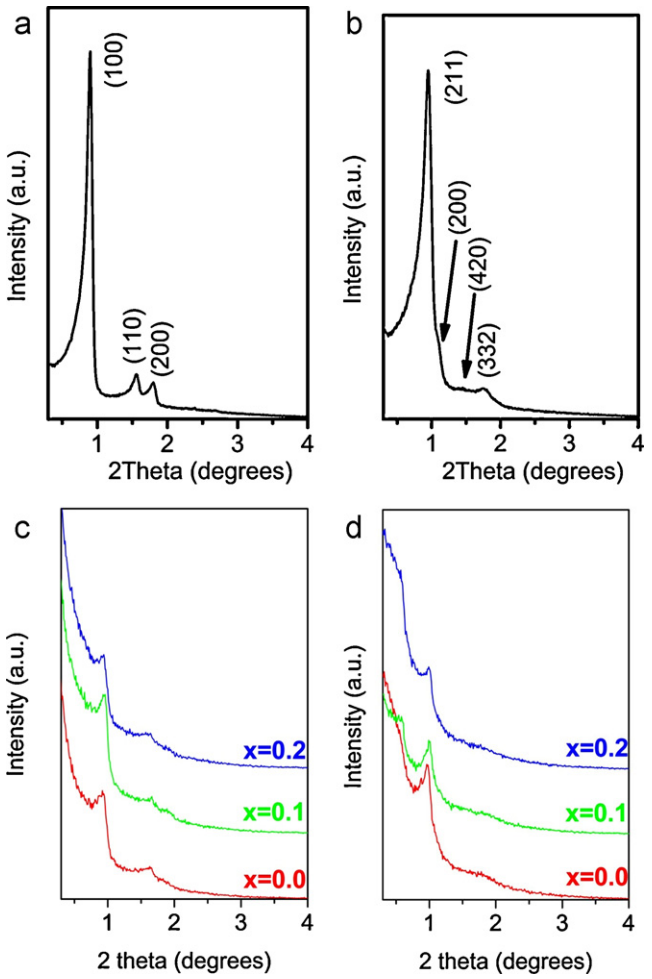

Fig. 1. Low angle XRD pattern of (a) SBA-15 silica and (b) KIT-6 silica, characteristic peaks of the structures are indicated. (c) $Ce_{1-x}Zr_xO_2$ SBA-15 replica and (d) $Ce_{1-x}Zr_xO_2$ KIT-6 replica, *x* indicated in the figure. $Ce_{1-x}Zr_xO_2$ samples were calcined at 800 °C.

is considered as OSC of the samples represented in μmol O_2/g catalyst.

3. Results

3.1. Obtention of mesoporous oxides

Low angle XRD analysis of the templates confirmed the formation of mesoporous structures. In the case of SBA-15, Fig. 1(a) presents the reflections of the two-dimensional *p6mm* hexagonal distribution of the pores, with a pore size around 9.8 nm. The diffraction pattern for KIT-6 (Fig. 1(b)) corresponds to a three dimensional *Ia3d* cubic mesostructure, the size of the pores is slightly smaller than SBA-15, being around 9.2 nm. The results are in agreement with those reported earlier [11,13].

Results from $Ce_{1-x}Zr_xO_2$ in its both forms, SBA-15 and KIT-6, calcined at 800 °C (Fig. 1(c) and (d)) reveal characteristic peaks of the same space groups as the templates and thus, they conserve the original mesostructure as it expected. KIT-6 replicas show an additional reflection at 0.5° which is related to the uncoupled framework during the replication process, as discussed by Rossinyol et al. [19]. For both replicas, the main reflection is slightly displaced to a higher angle, being the associated nominal size of the replicas 0.4 nm smaller than the corresponding porous size of the template.

Table 1
BET surface area of samples calcined at 800 °C.

%Zr	Surface area (m^2/g)	
	SBA-15	KIT-6
0	105.0	111.3
10	121.2	126.3
20	123.3	128.3

TEM images (Fig. 2) further corroborate the transferred porosity from the template to the mesoporous oxide. It is worthy observe that the mesoporous oxide, whether in its pure form (Fig. 2(a) and (b)) or as ceria–zirconia solid solution (Fig. 2(c)) structures are kept despite the samples were calcined at high temperatures even at 1000 °C. As it can be seen in the micrographs, SBA-15 and KIT-6 replicas present morphology completely different. SBA-15 replica consists of an array of nanorods or nanowires composed for aligned nanocrystals of ceria or ceria–zirconia, with a diameter of around 9.4 nm. For KIT-6 replica, the nanocrystals form a nanostructure which resembles a three dimensional network, with a more open porosity. Results from BET surface area (Table 1) reflects this tendency, being the surface area of KIT-6 replicas 5% higher than the same samples obtained as SBA-15 replicas. Furthermore, for both templates, as zirconium is introduced, there is an increment of surface area related to the diminution of the crystallite size discussed in the next section, Fig. 3.

3.2. Solid solution $Ce_{1-x}Zr_xO_2$

The formation of a fluorite solid solution was analysed by XRD. Calcination of the materials at 600 °C did not yield to fully crystalline materials (not indicated here). At 1000 °C, on the other hand, results were similar to those obtained at 800 °C. Therefore, we will mainly focus on characterization and properties of the material obtained at 800 °C. Fig. 4 shows the patterns of the samples in a wide range of compositions, up to 50%Zr. For pure ceria, the pattern includes the typical reflections of the fluorite structure with peaks located at 28.5, 33.1, 47.6, 56.5, and 59.2 corresponding to (1 1 1), (2 0 0), (2 2 0), (3 1 1), and (2 2 2) respectively [20], according to the JCPDS card 34-0394. As a result of the substitution of Ce^{4+} ions (0.97 Å) with Zr^{4+} ions (0.84 Å) which has a smaller diameter, there is a compression of the cell parameter "*a*" for the cubic structure. Therefore, a slight shift to higher angles is found in the characteristic peaks of the samples as the zirconium concentration is increased (from pure ceria to 50% zirconia). It discloses the fact that the $Ce_{1-x}Zr_xO_2$ solid solution is formed. This behaviour is found for both structures (KIT-6 and SBA-15) in the temperature range under investigation.

Focusing on the peak centred at 47.5°, which corresponds to the (2 2 0) reflection of the fluorite structure, it is clearly seen that for Zr contents of 0.35 and higher, a new shoulder in the peak appears which indicates that at such high concentrations of Zr, a secondary phase is being formed, which was further confirmed through Raman spectroscopy tests.

Based on the phase diagram of CeO_2–ZrO_2, solid solutions containing low concentrations of ZrO_2 (<15%), present a cubic fluorite structure (*Fm3m*) [21]. However, with increasing zirconia content, new tetragonal phases start to appear especially for those calcined at high temperatures.

Studies on phase transitions in CeO_2–ZrO_2 system by Yashima et al. [22] revealed the fact that secondary phases (with tetragonal structure) can be formed depending on thermodynamic conditions and composition of the solid solution. On the other hand, Zhang et al. showed that the presence of the secondary phase is a function of nanoparticle size [21] and varies for different processes applied by various researchers. In other words, decreasing particle size

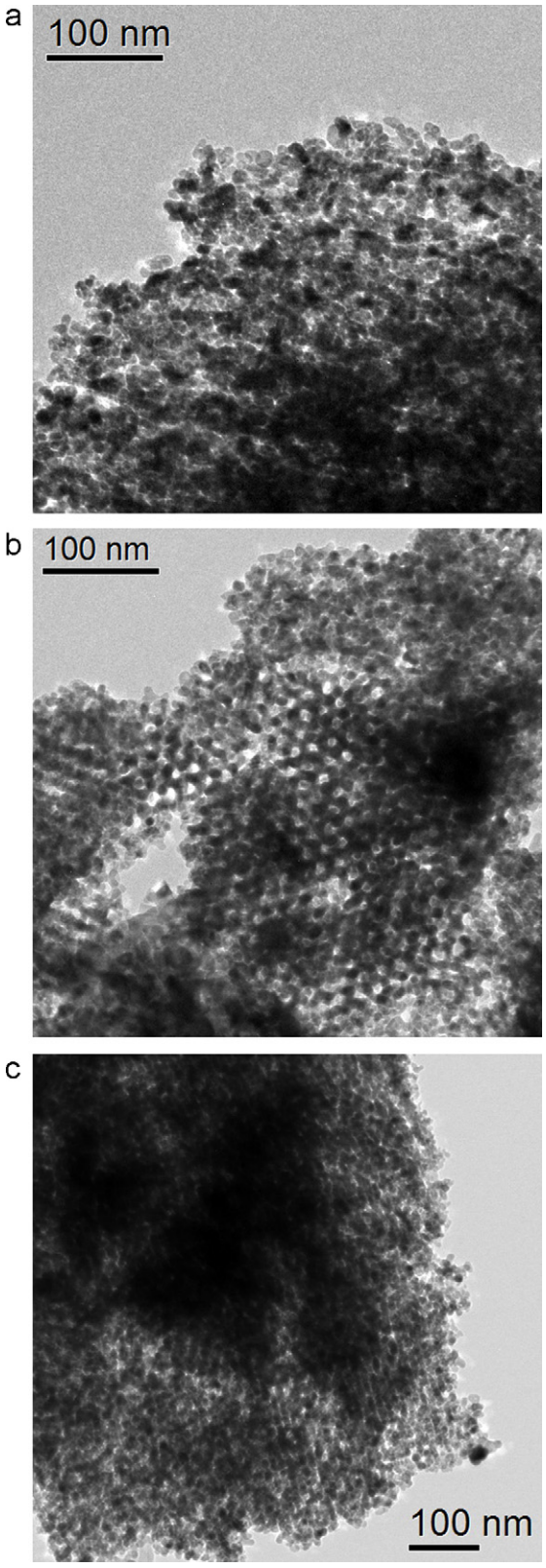

Fig. 2. TEM images of (a) pure CeO_2 (SBA-15) calcined at 1000 °C. (b) Pure CeO_2 (KIT-6) calcined at 1000 °C. (c) Ceria–zirconia (KIT-6, $x = 20\%$) calcined at 800 °C. The ordered mesostructure is clearly seen in these images. The small particle size and highly porous structure shows that the template has been successful in preventing grain growth at high temperature.

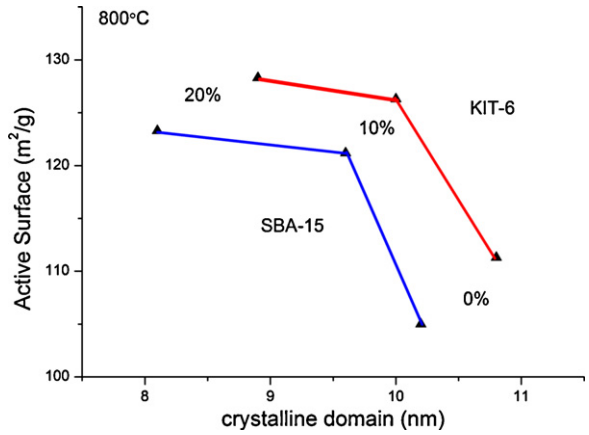

Fig. 3. Active surface area (blue SBA15 and red KIT-6) versus crystalline domain size determined from XRD measurements. The larger surface area revealed by KIT-6 is due to its complex 3D structure.

affects the phase stability shifting the onset of secondary phase formation to higher contents of zirconia. Thus, phase diagrams are not applicable to every process and condition since they are sketched under equilibrium conditions. So, the effect of particle size may not be neglected.

However, in our samples calcined at 1000 °C, higher concentrations of Zr (above 20%) seem not to promote solid solution formation as no shift in the patterns is observed. This has been already explained by phase segregation which shows its highest tendency at this temperature [20].

Concerning the shift in the diffraction pattern with increasing the zirconium content, the cell "*a*" parameter values were calculated by adjusting the profile using Fullprof program [23] taking into account a single phase with fluorite symmetry. Results are shown in Fig. 5. They point out the evolution of cell parameter of $Ce_{1-x}Zr_xO_2$ (for both SBA-15 and KIT-6 structures) for various concentrations. In the interval 0–20%, the dependence of the cell parameter with zirconium content is linear, confirming that a solid solution is formed. At higher concentrations, there are some discrepancies in the calculation of the cell parameter due to the overlapping between the different phase contributions.

The average crystallite size was calculated using Scherrer formula from the FWHM (full width at half maximum) of (1 1 1)

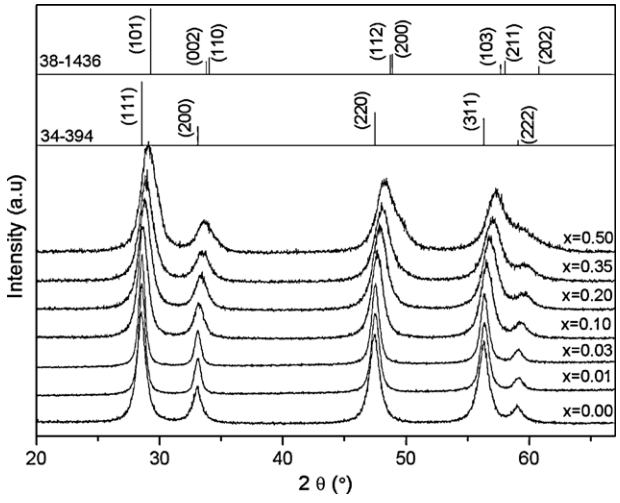

Fig. 4. XRD of SBA-15 $Ce_{1-x}Zr_xO_2$ with x from 0 to 0.5. Indexed patterns corresponds to cubic fluorite CeO_2 (JCPDS 34-394) and tetragonal $Ce_{0.5}Zr_{0.5}O_2$ (JCPDS 38-1436). The small shift in peak positions due to the formation of solid solution is quite obvious.

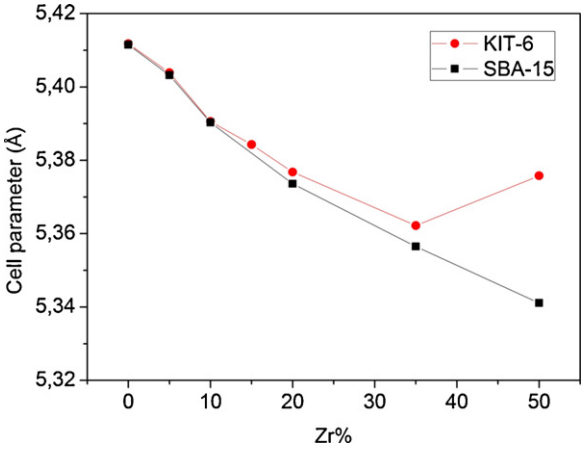

Fig. 5. Cell parameter as a function of Zr content. The reduction of cell parameter with increasing Zr-content is a result of substitution of Ce^{4+} ions with smaller Zr^{4+} ions.

Table 2
Crystallite size of the mesoporous materials calculated based on Scherrer formula.

Sample	Template	600 °C	800 °C	1000 °C
CeO_2	SBA-15	8.1	10.2	17.7
$Ce_{0.9}Zr_{0.1}O_2$	SBA-15	–	9.6	13.1
$Ce_{0.8}Zr_{0.2}O_2$	SBA-15	–	8.1	11.7
CeO_2	KIT-6	8.8	10.8	21.2
$Ce_{0.9}Zr_{0.1}O_2$	KIT-6	9.2	10.0	13.3
$Ce_{0.8}Zr_{0.2}O_2$	KIT-6	7.9	8.9	12.3

reflection of the cubic fluorite structure. Results are summarised in Table 2 and correlated in Fig. 6. The XRD estimated crystallite domain sizes are useful to compare the effects of composition and calcination temperature on the different samples, but it is necessary to keep in mind that the silica hard template helps us to maintain the overall porosity and the grain growth takes place just inside the pores. The introduction of zirconia in the ceria lattice likely promotes the formation of defects and it limits the growth rate, resulting to a smaller crystalline domain sizes such it is shown in the plot of Fig. 7. Likewise, as the temperature increases, the crystalline domains increased too. It becomes much more important at 1000 °C as compared to lower temperatures. Finally, under the same conditions, KIT-6 templated materials showed a slightly higher crystalline size, 0.4 nm, than SBA-15 templated materials. This can be attributed to the fact that the 3D distribution of pores of KIT-6 allows grain growth by coalescence of neighbour nanocrystal with

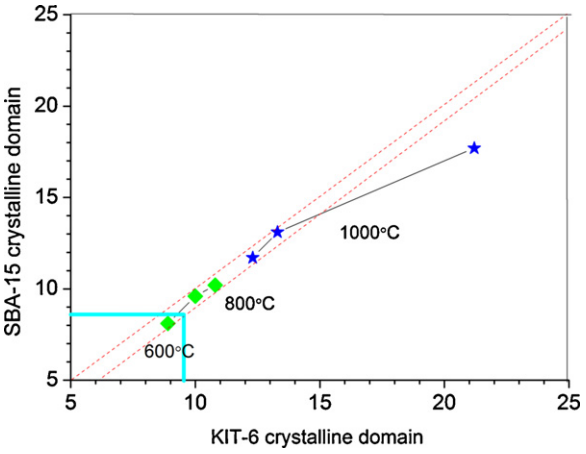

Fig. 6. Relation between the obtained parameters of the SBA-15 and KIT-6.

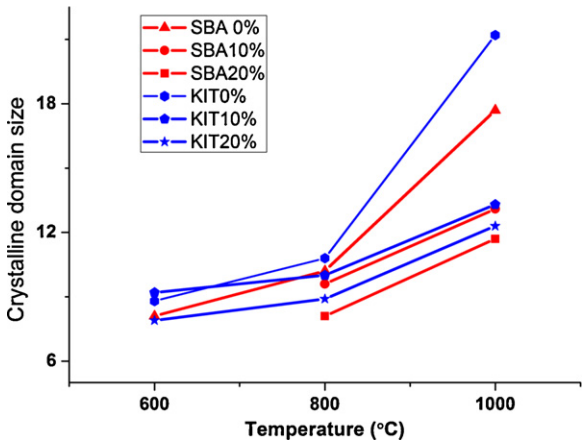

Fig. 7. Variation of crystallite domain size with temperature (for KIT-6 and SBA-15).

less difficulties than for a SBA-15 structure where the grain growth is limited to 1 direction along the pore, forming a nanorod like shaped crystal. It should be remarked that at 1000 °C this growth mechanisms associated to the available porous shape justifies why KIT-6 pure ceria present a much more important growth than SBA-15 pure ceria and for both the growth is much more significant than pure ceria growth is not limited for the presence of zirconia, Fig. 7.

In order to confirm the results from XRD, the samples were analysed by Raman spectroscopy. For a pure CeO_2 with cubic fluorite structure it is expected just one active Raman mode (F_{2g}) centred at 464 cm^{-1} whereas for the tetragonal phase, with space group $P4_2/nmc$, six Raman modes near 131, 247, 307, 464, 596 and 626 cm^{-1} are allowed [22]. Fig. 8 shows the Raman spectra of ceria and ceria–zirconia samples in a wide range of compositions. As it can be seen, at concentrations up to 20%, a strong peak at around 464 cm^{-1} belonging to the fluorite structure starts to appear. Due to the replacement of Ce ions by Zr ones, which results in shorter M–O bonds, the position of the peak (Fig. 9) moves slightly to higher frequencies, which confirms the formation of the solid solution. Furthermore, the incorporation of zirconium widens the peak due to the small crystalline domain and the introduction of some defects in the structure. For the sample with 20%Zr, it can be also seen a less prominent and broad band near 600 cm^{-1} which is a defect-induced LO mode of ceria due to relaxation of symmetry rules, assigned to defect spaces with an octahedral symmetry that

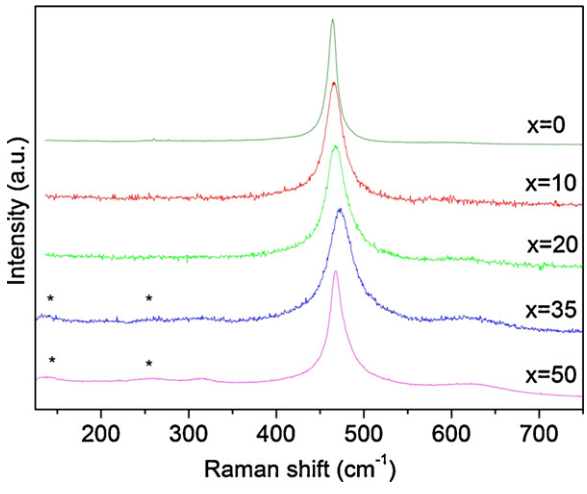

Fig. 8. Raman spectra for $Ce_{1-x}Zr_xO_2$ samples with KIT-6 structure, calcined at 800 °C. Formation of tetragonal phase is confirmed for Zr-contents higher than 20%.

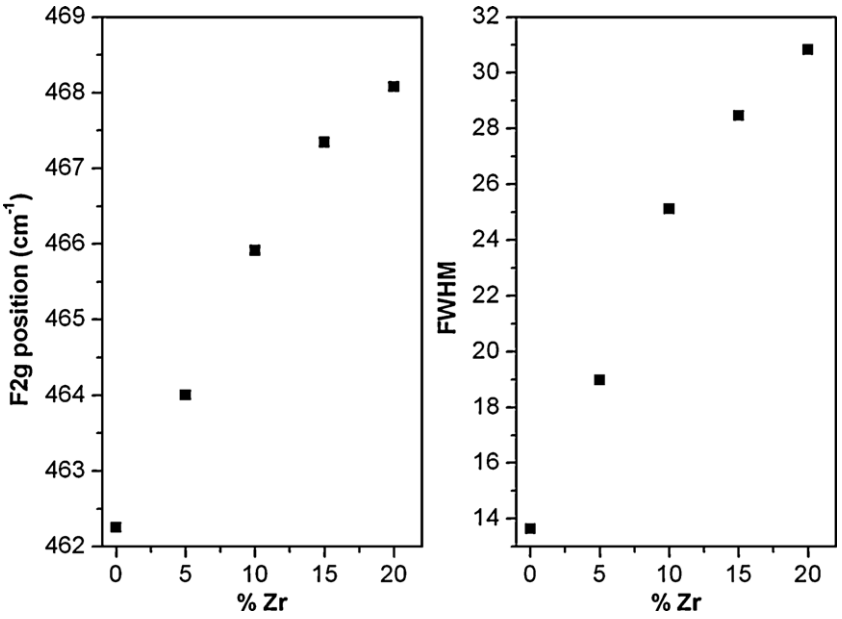

Fig. 9. Position and FWHM (full width at half maximum) of F_{2g} Raman mode for $Ce_{1-x}Zr_xO_2$ samples with KIT-6 structure, calcined at 800 °C. Increasing FWHM with increasing Zr-content is due to the crystal shrinkage with addition of Zr^{4+} ions.

includes a dopant cation (Zr) in the eightfold coordination of oxygen [11,24,25].

For high concentrations of zirconia, the Raman spectra slightly changes, appearing new peaks (indicated by stars in Fig. 8) at 131, 307 and 596 cm^{-1} which belong to tetragonal zirconia with $P4_2/nmc$ space group. For a 50%Zr, which is mainly tetragonal, the vibration at 464 cm^{-1} is not displaced to higher frequencies, since it is not assigned to the F_{2g} mode of fluorite but corresponds to the tetragonal phase.

3.3. Functional characterization

In order to explore the possibility to use these materials as oxygen sensors or in three way catalysts, oxygen storage capacity was measured. An example of the thermogravimetry analysis results is shown in Fig. 10. Weight gain of the material as a result of exposure to air ascribed to oxygen uptake can be clearly seen. Results, presented in Fig. 11 (for SBA-15 templated material calcined at 800 °C), show that solely with the addition of 5% of zirconia, OSC increases to a large extent, around a factor 30. However, in the range from 5% to 20%, it seems that more zirconium content does not change OSC largely though it keeps its high level. This high OSC value suggests the uniform distribution of Zr atoms in the parent ceria lattice [26,27].

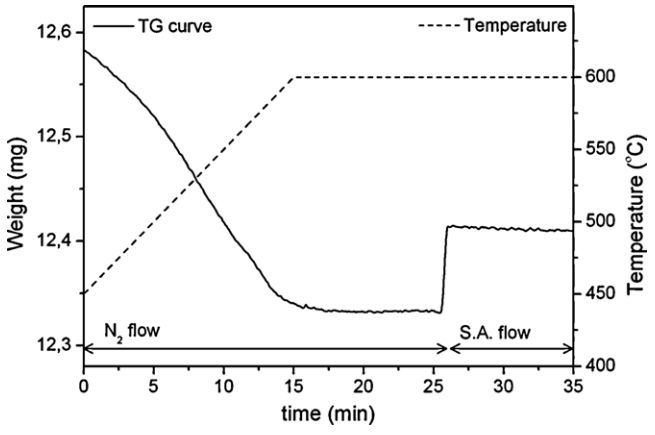

Fig. 10. TG curve for $Ce_{.8}Zr_{.2}O_2$ with SBA-15 structure, calcined at 800 °C.

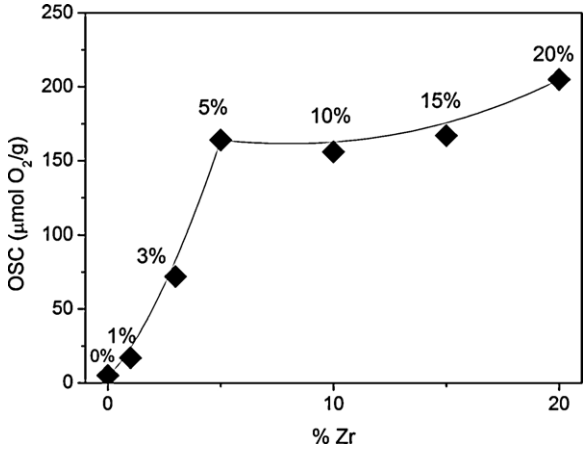

Fig. 11. Oxygen storage capacity of the materials as a function of Zr content.

4. Conclusions

Mesoporous ceria–zirconia solid solutions were synthesized via hard template method. Low angle XRD and TEM confirms the mesoporous nature of the oxides. It allows obtaining mesoporous oxides with a large surface area around 125 m^2/g. BET values for KIT-6 replicas slightly higher than the corresponding SBA-15 replicas.

Shifts in characteristic peaks of XRD pattern indicate that zirconia is incorporated into the ceria lattice in its cubic phase, in the interval 0–20%Zr, which was further corroborated by Raman spectroscopy. It was also confirmed the formation of tetragonal phase, which is not suitable for accommodating oxygen ions, at concentrations above 20%Zr. The incorporation of zirconium improves drastically its oxygen storage capacity.

Acknowledgements

This work has been financially supported through project MAT-2010-21510 "NANO-EN-ESTO" and by XaRMAE (Center of

Advanced Materials for Energy of the Generalitat de Catalunya). The authors thank R. Barbas of the plataforma the polimorfisme i calorimetria (SCT-UB) for providing TG results. T. Andreu thanks the DIUE of the Generalitat de Catalunya for the Beatriu de Pinós grant.

Appendix A. Supplementary data

Supplementary data associated with this article can be found, in the online version, at doi:10.1016/j.apcatb.2011.07.038.

References

[1] A. Martinez-Arias, G. Fernandez, M.C. Belver, J.C. Conesa, J. Soria, Catalysis Letters 65 (2000) 197.
[2] H. Sobukawa, R&D Review of Toyota CRDL 37 (2002) 1.
[3] S. Matsumoto, Toyota Technical Review 44 (1994) 10.
[4] L.C. Eduardo, d. G.J.A.A. Soler-Illia, A. Bouchara, D. Grosso, D. Durand, C. Sanchez, Angewandte Chemie International Edition 42 (2003) 347.
[5] N. Yasutaka, N. Takamasa, S. Akihido, S. Masahiro, R&D Review of Toyota CRDL 37 (2002) 20.
[6] A. Adamski, E. Tabor, B. Gil, Z. Sojka, Catalysis Today 119 (2007) 114.
[7] Y.-M. Chiang, E.B. Lavik, D.A. Blom, Nanostructured Materials 9 (1997) 633.
[8] S. Basu, P.S. Devi, H.S. Maiti, Journal of Materials Research 19 (2004) 3162.
[9] M. Fernandez-Garcia, A. Martinez-Arias, A. Iglesias-Juez, C. Belver, A.B. Hungria, J.C. Conesa, J. Soria, Journal of Catalysis 194 (2000) 385.
[10] E.B. Lavik, I. Kosacki, H.L. Tuller, Y.M. Chiang, J.Y. Ying, Journal of Electroceramics 1 (1997) 7.
[11] B. Reddy, A. Khan, Catalysis Surveys from Asia 9 (2005) 155.
[12] S. Enzo, R. Frattini, F. Delogu, A. Primavera, A. Trovarelli, Nanostructured Materials 12 (1999) 673.
[13] C. Liang, J. Qiu, Z. Li, C. Li, Nanotechnology 15 (2004) 843.
[14] V.N. Morris, R.A. Farrell, A.M. Sexton, M.A. Morris, Journal of Physics: Conference Series 26 (2006) 119.
[15] L. Fernández-Romero, J.M. Montero-Moreno, E. Pellicer, F. Peiró, A. Corneta, J.R. Morante, M. Sarret, C. Müller, Materials Chemistry and Physics 111 (2008) 542.
[16] E. Rossinyol, J. Arbiol, F. Peiro, A. Cornet, J.R. Morante, B. Tian, T. Bo, D. Zhao, Sensors and Actuators B: Chemical 109 (2005) 57.
[17] D. Zhao, J. Feng, Q. Huo, N. Melosh, G.H. Fredrickson, B.F. Chmelka, G.D. Stucky, Science 279 (1998) 548.
[18] F. Kleitz, S.H. Choi, R. Ryoo, Chemical Communications (2003) 2136.
[19] E. Rossinyol, J. Arbiol, F. Peiro, A. Cornet, J.R. Morante, L.A. Solovyov, B. Tian, D. Zhao, Microscopy of Semiconducting Materials 107 (2005) 333.
[20] I. Atribak, A. Bueno-Lopez, A. Garcia-Garcia, Catalysis Communications 9 (2008) 250.
[21] F. Zhang, C.-H. Chen, J.C. Hanson, R.D. Robinson, I.P. Herman, S.-W. Chan, Journal of the American Ceramic Society 89 (2006) 1028.
[22] M. Yashima, H. Arashi, M. Kakihana, M. Yoshimura, Journal of the American Ceramic Society 77 (1994) 1067.
[23] J. Rodriguez-Carvajal, Physica B 192 (1993) 55.
[24] A. Nakajima, A. Yoshihara, M. Ishigame, Physical Review B 50 (1994) 13297.
[25] M. Balaji Prasad, G. Vinita, R. Mainak, T. Avesh Kumar, Journal of the American Ceramic Society 90 (2007) 2961.
[26] S. Damyanova, B. Pawelec, K. Arishtirova, M.V.M. Huerta, J.L.G. Fierro, Applied Catalysis A: General 337 (2008) 86.
[27] A. Suda, K. Yamamura, A. Morikawa, Y. Nagai, H. Sobukawa, Y. Ukyo, H. Shinjo, Journal of Materials Science 43 (2008) 2258.